Received: 8 April 2025 | Revised: 14 May 2025 | Accepted: 7 June 2025

DOI: 10.1002/dug2.70058

RESEARCH ARTICLE

DUSE WILEY

A rock brittleness index based on the postpeak energy release rate and damage surface characteristics for brittle hard rock

Biao Wang[1] | **Zaobao Liu**[1] | **Jing Xue**[2] | **Bo Lu**[1,3] | **Wei Zeng**[4] | **Dengke Zhang**[5]

[1]State Key Laboratory of Intelligent Deep Metal Mining and Equipment, Northeastern University, Shenyang, China

[2]CAEA Innovation Center for Geological Disposal of High-Level Radioactive Waste, Beijing Research Institute of Uranium Geology, Beijing, China

[3]Department of Engineering, University of Cambridge, Cambridge, UK

[4]State Key Laboratory of Intelligent Construction and Healthy Operation and Maintenance of Deep Underground Engineering, China University of Mining and Technology, Xuzhou, China

[5]State Key Laboratory of Disaster Prevention and Mitigation of Explosion & Impact, Army Engineering University of PLA, Nanjing, China

Correspondence

Zaobao Liu, State Key Laboratory of Intelligent Deep Metal Mining and Equipment, Northeastern University, Shenyang 110819, China.
Email: liuzaobao@mail.neu.edu.cn

Funding information

Natural Science Foundation of China, Grant/Award Number: 52278333; China Atomic Energy Authority (CAEA) for China's URL Development Program, the Geological Disposal Program

Abstract

Rock brittleness is an important mechanical property that describes damage of rocks. This study proposes a rock brittleness evaluation index considering the postpeak energy release rate and damage surface morphology parameters. The accuracy of the brittleness index is verified by the triaxial direct shear test of granite under different confining pressures. By comparing the accuracy and precision of eight existing brittleness evaluation indexes, the results show that BI_{PERF} can more accurately evaluate the postpeak brittleness of granite under direct shear conditions. The findings confirm that the brittleness of Beishan granite decreases with increasing confining pressure, with BI_{PERF} declining by 23.5% as the confining pressure increases from 2 to 22 MPa. Similarly, brittleness decreases with increasing temperature, with BI_{PERF} decreasing by 20.16% as the temperature increases from 30 to 110°C. The research findings provide significant guidance for evaluating the stability of engineering rock masses and predicting geological hazard risks.

KEYWORDS

brittleness index, energy evolution, thermal–mechanical coupling, triaxial direct shear

Highlights

- The energy evolution of Beishan granite under high-temperature and high-stress triaxial direct shear (TDS) conditions is obtained.
- Damage surface characterization of Beishan granite under high-temperature and high-stress TDS conditions is determined.
- A new rock brittleness index is established to describe the energy evolution of granite under TDS conditions.
- Beishan granite brittleness under TDS conditions at high temperatures in real time is obtained.

1 | INTRODUCTION

Rock brittleness is an important mechanical property that describes the damage of rocks (Gong & Wang, 2022; Liu, Wang, et al., 2023; Meng et al., 2021), and it is crucial in many fields such as petroleum engineering, geotechnical engineering, and geohazard research (Rahimzadeh Kivi et al., 2018; Zhao et al., 2020). Stability problems in rock excavation (Hajiabdolmajid & Kaiser, 2003; Meng et al., 2015), hydraulic fracturing for unconventional energy sources (Wang et al., 2021; Zhang et al., 2016), tunnel boring machine cutter wear for hard rock excavation (Zhang et al., 2024), and rockbursts in underground engineering (Kidybiński, 1981; Singh, 1986; Zhao et al., 2021) involve brittleness evaluations.

The rock brittleness index is a key parameter when evaluating the damage characteristics of a rock (Altindag, 2002; Meng et al., 2021; Tarasov, 2023). The violent damage process usually indicates high brittleness of the rock (Kahraman & Altindag, 2004; Nejati & Moosavi, 2017; Yarali & Kahraman, 2011). However, the method of measuring and calculating the brittleness of rocks has not led to a unified standard and calculation method. Table 1 lists the common brittleness calculation methods in some fields. Rock brittleness indices are defined in various forms such as the strength ratio, the modulus ratio, and the energy index ratio (Meng et al., 2015; Zhang et al., 2016). Although brittleness indices have been widely used in different areas of rock engineering, there is no consensus on the definition and

TABLE 1 Summary of commonly used brittleness indexes.

Methods	Definition	Description	Source
Based on rock mineral constituents	$BI_1 = \frac{W_{qtz}}{W_{qtz+carb+cly}}$	Wx indicate weight fraction of component x, qtz = quartz, carb = carbonate, cly = clay, dol = dolomite, TOC = total organic carbon QFM = quartz + feldspar + mica QFP = quartz + feldspar + pyrite	Jarvie et al. (2007)
	$BI_2 = \frac{W_{qtz+dol}}{W_{qtz+carb+cly+TOC}}$		Wang and Gale (2009)
	$BI_3 = \frac{W_{QFM+carb}}{W_{total}}$		Jin et al. (2015)
Based on hardness	$BI_4 = \frac{H}{K_{IC}}$	H is the hardness, K_{IC} is the mode I fracture toughness, C is the characteristic crack length, and a is the indent size for Vickers indents at a specified load.	Lawn and Marshall (1979)
	$BI_5 = \frac{HE}{K_{IC}^2}$		Quinn and Quinn (1997)
	$BI_6 = \frac{C}{a}$		Sehgal et al. (1995)
Based on the strength parameter	$BI_7 = \frac{\sigma_c}{\sigma_t}$	σ_c and σ_t are the uniaxial compressive strength and the tensile strength, respectively	Hucka and Das (1974)
	$BI_8 = \frac{\sigma_c - \sigma_t}{\sigma_c + \sigma_t}$		Hucka and Das (1974)
	$BI_9 = \sigma_c\sigma_t/2$		Altindag (2003)
	$BI_{10} = \sqrt{\sigma_c\sigma_t/2}$		Altindag (2010)
Based on the stress–strain curve	$BI_{11} = (\tau_p - \tau_r)/\tau_p$	τ_p and τ_r are the peak and residual strengths, respectively, ε_e and ε_t are the reversible (or elastic) and total strains at failure, respectively, ε_p is the sustained plastic strain at failure, ε_r is the residual strain, U_e, U_{total}, $U_{peak,}$ and U_{post} are the elastic energy, the total elastic energy, the total energy at peak, and the rupture energy, respectively.	Bishop (1967)
	$BI_{12} = (\varepsilon_r - \varepsilon_e)/\varepsilon_r$		Andreev (1995)
	$BI_{13} = \varepsilon_d$		Andreev (1995)
	$BI_{14} = \varepsilon_e/\varepsilon_t$		Hucka and Das (1974)
	$BI_{15} = (\varepsilon_t - \varepsilon_e)/\varepsilon_t$		Andreev (1995)
	$BI_{16} = 1/\varepsilon_e$		Gong and Sun (2015)
	$BI_{17} = \sigma_c/\varepsilon_s$		Liang et al. (2017)
	$BI_{18} = U_e/U_{total}$		Hucka and Das (1974)
	$BI_{19} = U_e/U_{post}$		Munoz et al. (2016)
	$BI_{20} = U_{peak}/U_{total}$		Munoz et al. (2016)

measurement of rock brittleness (Meng et al., 2021). The method combining energy coefficients is the most widely used one (Gong et al., 2024; Munoz et al., 2016; Rahimzadeh Kivi et al., 2018; Wang et al., 2020; Zhang et al., 2022). The nature of rock damage is an irreversible transformation process driven by energy; the process involves energy absorption, energy storage, and energy dissipation, and the energy evolution mechanism is closely related to the microcracks and damage states within the rock (Feng et al., 2024; Wang et al., 2023; Zhang et al., 2019). It has been suggested that rock brittleness indicators should be characterized by simultaneous damage surfaces (Liu, Wang, et al., 2023).

A reliable scientific rock brittleness evaluation index should cover the whole process of rock rupture, and the variability of the rock rupture surface, subjected to nonhomogeneity and anisotropy, should also be considered. To fill the existing research gap, this study analyzes the energy evolution law of the stress–strain curve on the whole process of rock rupture through the triaxial direct shear (TDS) test of rock, investigates the effect of different circumferential pressure and temperature conditions on the randomness of the breaking surface, and proposes a new evaluation index of rock brittleness based on the principle of energy and the effect of the randomness of the breaking surface on rock damage. The reliability and accuracy of the new indicators were verified through experimental validation and comparison with existing calculation methods.

2 | BRITTLENESS INDEX FOR DAMAGE OF BRITTLE HARD ROCK

2.1 | Energy analysis of shear failure

Failure of rocks is the result of accumulating internal damage and is essentially a change in energy (Gong et al., 2024; He et al., 2018; Xie et al., 2011). To characterize the brittleness of rock shear failure, the energy evolution process of rock shear damage was analyzed as is shown in Figure 1. In the prepeak phase, most of the external input energy is stored within the rock as elastic strain energy, and a small portion of the external input energy is dissipated in the form of plastic deformation. Upon arrival at the postpeak phase, most of the external input energy and the internal energy stored in the rock is violently released with the onset of the damage and a small portion of the remaining energy is

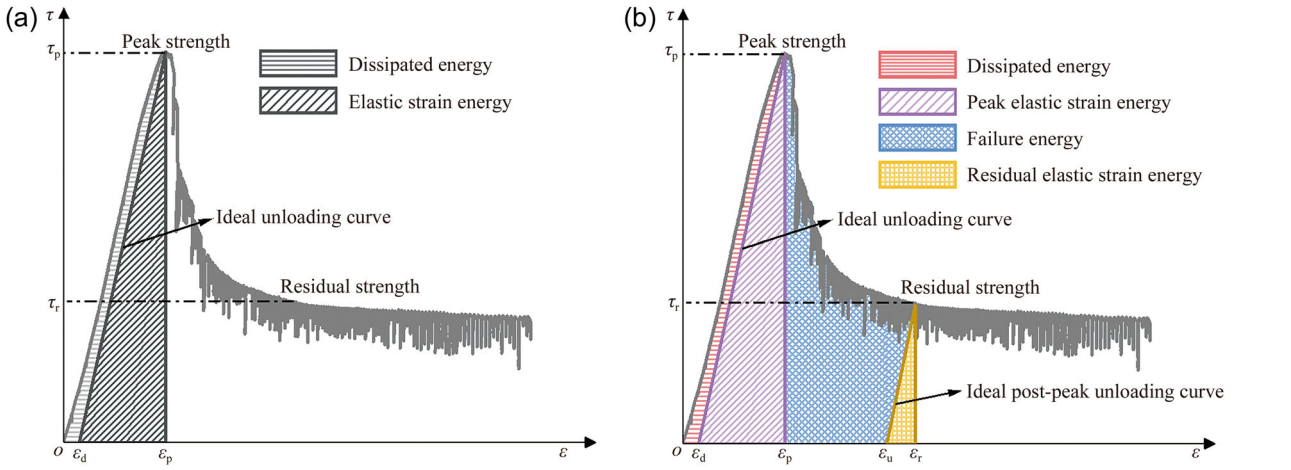

FIGURE 1 Characteristics of energy evolution in the triaxial direct shear failure process. (a) Schematic diagram of elastic strain energy and dissipated energy and (b) schematic diagram of the division of energy types.

stored in the rock in the form of residual elastic strain energy. The method of dividing the energy of each part is shown in Figure 1, and the calculation method is shown in Equations (1)–(9).

As illustrated in Figure 1a, the total energy input throughout the entire experimental process is

$$U_{\text{total}} = U_{\text{e}} + U_{\text{d}}. \tag{1}$$

The total density of U_{total} can be calculated using Equation (2).

$$U_{\text{total}} = \int_0^{\varepsilon_1} \tau d\varepsilon + 2\int_0^{\varepsilon_3} \sigma_3 d\varepsilon. \tag{2}$$

The elastic strain energy density U_{e} is determined using Equation (3).

$$U_{\text{e}} = \frac{1}{2E_0}\left[\sigma_1^2 + 2\sigma_3^2 - 2v\left(\sigma_3^2 + 2\sigma_1\sigma_3\right)\right]. \tag{3}$$

The dissipated energy density U_{d} is expressed as

$$U_{\text{d}} = U_{\text{total}} - U_{\text{e}}. \tag{4}$$

To further investigate the influence of postpeak behavior, the energy is subdivided as shown in Figure 1b. The prepeak elastic strain energy density is

$$U_{\text{p}}^{\text{e}} = \frac{{\tau_{\text{p}}}^2}{2E_0}. \tag{5}$$

The residual elastic strain energy density is

$$U_{\text{r}}^{\text{e}} = \frac{{\tau_{\text{r}}}^2}{2E_0}. \tag{6}$$

The dissipated energy density is

$$U_{\text{d}} = \int_0^{\varepsilon_{\text{p}}} \tau \text{d}\varepsilon - \frac{{\tau_{\text{p}}}^2}{2E_0}. \tag{7}$$

The postpeak energy release rate

When $\varepsilon_{\text{p}} < \varepsilon_{\text{u}}$

$$U^{\text{f}} = \int_{\varepsilon_{\text{p}}}^{\varepsilon_{\text{r}}} \tau \text{d}\varepsilon - U_{\text{r}}^{\text{e}}, \tag{8}$$

When $\varepsilon_{\text{p}} > \varepsilon_{\text{u}}$

$$U^{\text{f}} = \int_{\varepsilon_{\text{p}}}^{\varepsilon_{\text{r}}} \tau d\varepsilon - U_{\text{r}}^{\text{e}} + \frac{E_0}{2}(\varepsilon_{\text{p}} - \varepsilon_{\text{u}})^2, \tag{9}$$

where U_{P}^{e} denotes the prepeak elastic strain energy density, U_{r}^{e} denotes the residual elastic strain energy density, U^{f} denotes the postpeak energy release rate, and U_{d} denotes the dissipated energy density. ε_{d}, ε_{p}, ε_{u}, and ε_{r} represent the prepeak plastic strain, the peak strain, the postpeak plastic strain, and the residual strain, respectively, E_0 denotes the elastic modulus, and v represents the Poisson's ratio (Figure 2).

2.2 | Morphological parameters of damaged surfaces

The joint roughness coefficient (*JRC*) values and joint matching coefficient (*JMC*) values are key parameters to characterize the surface roughness and match in geotechnical engineering. The *JRC* value can be calculated using Equations (10) and (11) according to the literature (Heinze et al., 2021). About 100 straight lines are taken in the x-direction at intervals of 0.5 mm to compute the *JRC* values in the y-direction. The *JRC* values of the samples are obtained by averaging all the straight-line *JRC* values in the y-direction. The *JMC* value is obtained from the ratio of the nodal contact area to the specimen cross-sectional area in Equation (12) (Zhao, 1997)

$$JRC = 32.2 + 32.47\log(Z_2), \tag{10}$$

$$Z_2 = \sqrt{\frac{1}{N-1}\sum_{i=2}^{N}\left(\frac{z_i - z_{i\text{-}1}}{x_i - x_{i\text{-}1}}\right)^2}, \tag{11}$$

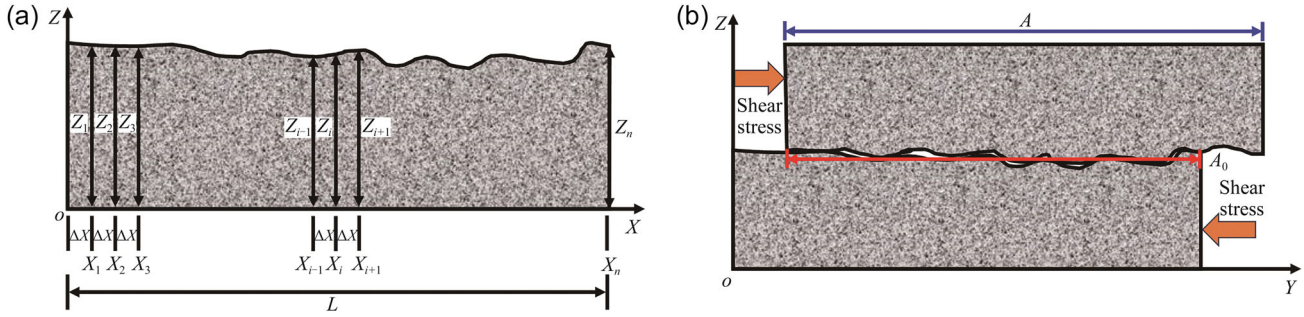

FIGURE 2 Acquisition of *JRC* and *JMC* values (Barton, 1976; Zhao, 1997). (a) Schematic diagram of the calculation method of *JRC* and (b) schematic diagram of the calculation method of *JMC*.

$$JMC = \frac{A_0}{A}, \tag{12}$$

where x_i is one of the N discrete points along the contour direction, z_i is the height value corresponding to the contour, A_0 is the nodal contact area, and A is the cross-sectional area of the specimen.

2.3 | A rock brittleness evaluation index

Brittleness is a very important property of engineering materials, which reflects the deformation and fracture characteristics of materials under stress. Several studies have shown that the postpeak energy release rate of a rock has a large influence on the brittleness of the rock, so the postpeak energy release rate should be regarded as an important influencing factor in the evaluation of rock brittleness. The roughness of the rock-damaged surface and the coincidence between the two sections also have some influence on the postpeak energy release. In order to better reflect the brittle damage evolution of rocks under TDS conditions, this study utilizes the rock brittleness evaluation indexes (BI_{PERF}) established by using the postpeak energy release rate of the rock and the characteristics of the damaged surface. The brittleness index calculation formula is shown in Equation (13) as follows:

$$B_{\mathrm{PERF}} = \sqrt{JRC \cdot JMC}\,\frac{U^{\mathrm{f}}}{U_{\mathrm{p}}^{\mathrm{e}}}. \tag{13}$$

3 | TDS TEST

Due to the experimental design of direct shear failure surfaces and the presence of free surfaces, the characteristics of triaxial stress in deep engineering are overlooked. Previous studies have shown that while triaxial compression tests account for triaxial stress conditions and have significantly contributed toward understanding rock shear strength and deformation, the failure surfaces in such tests show considerable uncertainty, often fragmenting into multiple pieces. This introduces potential errors in quantifying shear failure surface characteristics. To address this, we used a modified TDS apparatus to obtain more precise quantitative information on failure surfaces. Detailed information on the shear apparatus can be found in the referenced literature

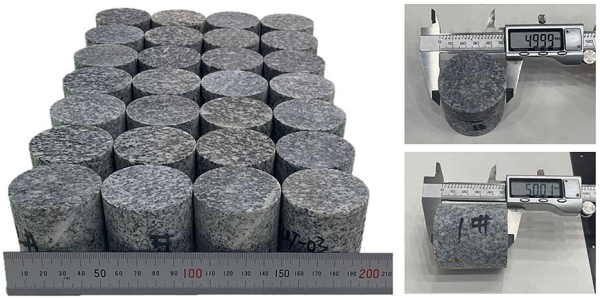

FIGURE 3 Granite specimen.

(Liu, Liu, et al., 2023). Granite from Beishan, Gansu Province, was selected for the TDS test to obtain the postpeak energy release rate and damage surface parameters of the rock to verify the brittleness index. The specimen size is processed into cylindrical specimens of 50 mm diameter and 50 mm height, as shown in Figure 3.

The test was carried out using the rock high-temperature and high-pressure TDS testing system of the Key Laboratory of the Ministry of Education for Safe Mining of Deep Metal Mines of Northeastern University (Figure 4). Geostress measurements indicate that the in situ stress at a depth of 560 m reaches approximately 20 MPa (Chen et al., 2023), while thermal analysis reveals that the rock mass barrier's peak temperature attains 110°C (Seo et al., 2024). A total of four different confining pressure levels were set up at 30°C (2, 9, 15, and 22 MPa), and five temperature levels were set up at 22 MPa confining pressure (30, 50, 70, 90, and 110°C) for a total of 24 sets of tests.

In the TDS tests, the shear indenter, the TDS device, and the specimen were assembled, with a lubricant applied to contact surfaces to minimize friction, and the assembly was encapsulated in a heat-shrinkable sleeve. The specimen was leveled horizontally on the base. Shear and circumferential linear variable differential transformer (LVDT) sensors were connected, and force and displacement sensors were calibrated and zero-adjusted to ensure proper measurement ranges. Oil injection was performed to apply confining pressure and temperature, which was increased to the target value at 5°C/min, held for 2 h, and then pressurized at 0.1 MPa/s. After stabilization, shear stress was applied at 0.02 mm/min until specimen failure. The deformation was measured using an LVDT sensor, and stress and deformation are calculated as shown in Equations (14)–(16).

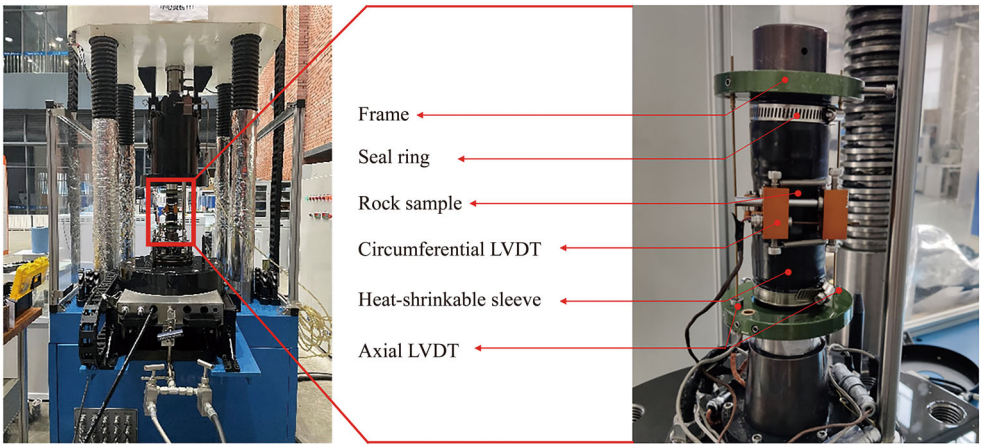

FIGURE 4 Rock high-temperature and high-pressure triaxial test system.

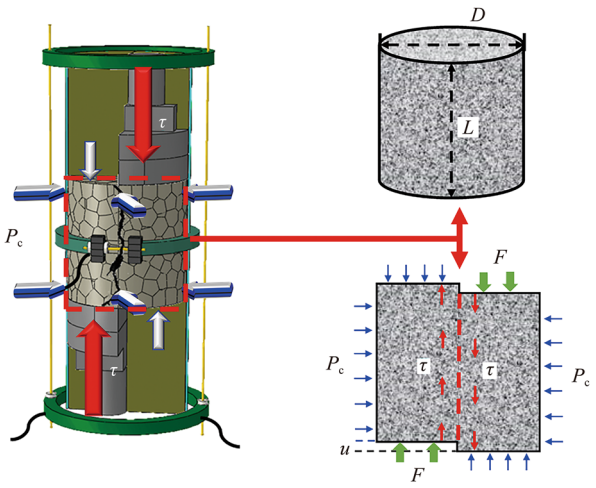

FIGURE 5 Schematic diagram of the force state and deformation of the specimen.

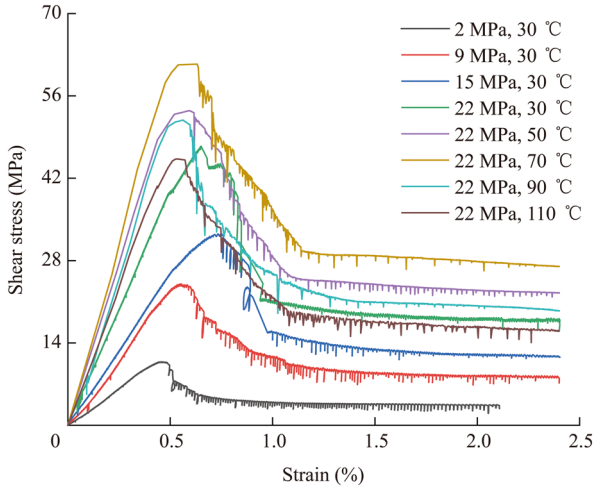

FIGURE 6 Triaxial direct shear stress–strain curves of Beishan granite.

$$\tau = \frac{F}{DL}, \tag{14}$$

where D (mm) is the diameter of the cylindrical specimen and L (mm) is the height of the cylindrical specimen.

Equation (11) represents the calculation of strain in the shear direction.

$$\chi = \frac{u}{L}. \tag{15}$$

Equation (12) represents the calculation of the circumferential strain (Figure 5).

$$\phi = \frac{\Delta D}{D}. \tag{16}$$

3.1 | Test results

The test results of the TDS of Beishan granite are shown in Figure 6, which indicate that the shear strength decreases with an increase in the confining pressure, and shows a trend of first increasing and then decreasing with an increase in the temperature. The stress–strain curves of direct shear failure are shown to have a more stable postpeak curve compared with the traditional triaxial compression test, and this phenomenon provides more convincing data support for the brittle characterization of postpeak rock damage. Peak and residual strengths are strongly influenced by the confining pressure and the temperature. Increasing the confining pressure from 2 to 22 MPa enhances the peak strength by 4.39 times and residual strength by 5.77 times. As shown in Figure 6, stress–strain curves demonstrate that both strengths initially increase and then decline with increasing temperature. Specifically, increasing the temperature from 30 to 70°C boosts peak and residual strengths by 30.15% and 45.33%, respectively. However, further increasing the temperature to 110°C reduces peak and residual strengths by 23.61% and 30.54%, respectively.

Based on Equations (1)–(5), the experimental results obtained from various energy values during TDS of granite from Beishan are shown in Table 2.

Table 2 shows that U_P^e and U_r^e will increase approximately linearly with increasing levels of confining

pressure; when the confining pressure increases from 2 to 22 MPa, U_P^e increases from 2.16 to 14.59 kJ/m^3, which is a 5.75-fold increase, and U_r^e increases from 0.31 to 2.68 kJ/m^3, which is a 7.65-fold increase. U_P^e and U_r^e are significantly affected by the confining pressure. U^f and U_d increase approximately linearly with increasing confining pressure when the confining pressure increases from 2 to 22 MPa; U^f increases from 2.55 to 12.04 kJ/m^3, which is a 3.72-fold increase. U_d increases from 0.63 to 4.82 kJ/m^3, which is a 6.65-fold increase. U^f and U_d are significantly affected by the confining pressure. U_P^e and U_r^e show an increasing and then a decreasing trend as the temperature increases.

When the temperature increases from 30 to 70°C, U_P^e increases from 14.59 to 17.29 kJ/m^3, which is an increase of 18.51%. U_r^e increases from 2.68 to 4.36 kJ/m^3, which is an increase of 62.69%. When the temperature increases from 70 to 110°C, U_P^e decreases from 17.29 to 13.86 kJ/m^3, which is a decrease of 19.84%, and U_r^e decreases from 4.36 to 2.87 kJ/m^3, which is a decrease of 34.17%. This shows that U_P^e and U_r^e are significantly affected by the temperature. U^f and U_d show an increasing and then a decreasing trend. When the temperature increases from 30 to 70°C, U^f increases from 12.04 to 13.06 kJ/m^3, which is an increase of 8.47%, and U_d increases from 4.82 to 5.57 kJ/m^3, which is an increase of 15.56%. When the temperature increases from 70 to 110°C, U^f decreases from 13.06 to 10.26 kJ/m^3, which is a decrease of 21.44%. U_d decreases from 5.57 to 4.14 kJ/m^3, which is a decrease of 25.67%. Thus, U^f and U_d are significantly affected by the temperature.

Prepeak elastic strain energy density, residual elastic strain energy density, postpeak energy release rate, and dissipated energy density are all linearly and positively correlated with the confining pressure. The residual elastic strain energy density and the dissipated energy density increased the most, by 7.65 and 6.65 times, respectively. Taking the thermal strengthening point as the demarcation, with an increase in the temperature, the prepeak elastic strain energy density, the residual elastic strain energy density, the postpeak energy release rate, and the dissipated energy density show the trend of increasing and then decreasing, and the prepeak elastic strain energy density and the residual elastic strain energy density at the thermal strengthening point show the greatest increase, with increases of 18.51% and 62.69%, respectively.

TABLE 2 Energy evolution of the different specimens tested.

Number	P_c (MPa)	T (°C)	U_P^e (kJ/m^3)	U_r^e (kJ/m^3)	U_d (kJ/m^3)	U^f (kJ/m^3)
BSSRT-01a	2	30	2.10	0.24	0.56	2.77
BSSRT-01b	2	30	2.41	0.41	0.83	2.62
BSSRT-01c	2	30	1.96	0.27	0.49	2.27
BSSRT-02a	9	30	5.77	1.05	1.33	7.16
BSSRT-02b	9	30	5.50	0.92	1.27	5.55
BSSRT-02c	9	30	6.66	1.13	0.94	5.57
BSSRT-03a	15	30	10.40	2.19	3.75	9.31
BSSRT-03b	15	30	10.43	1.22	4.40	6.47
BSSRT-03c	15	30	10.39	1.27	4.38	7.63
BSSRT-04a	22	30	15.09	2.84	4.62	12.32
BSSRT-04b	22	30	14.52	2.92	5.02	11.72
BSSRT-04c	22	30	14.15	2.28	4.81	12.08
BSSHM-01a	22	50	15.98	4.42	5.19	13.54
BSSHM-01b	22	50	16.34	3.31	5.08	11.92
BSSHM-01c	22	50	16.17	3.31	4.85	11.76
BSSHM-02a	22	70	17.50	4.44	6.03	13.88
BSSHM-02b	22	70	17.26	4.33	5.76	12.84
BSSHM-02c	22	70	17.11	4.30	4.92	12.47
BSSHM-03a	22	90	13.97	4.02	4.20	11.79
BSSHM-03b	22	90	14.81	3.12	4.47	10.95
BSSHM-03c	22	90	15.36	2.99	4.88	10.55
BSSHM-04a	22	110	12.89	3.42	4.38	10.83
BSSHM-04b	22	110	14.04	2.38	4.31	10.28
BSSHM-04c	22	110	14.66	2.82	3.73	9.68

3.2 | Energy evolution

Figure 7 illustrates the energy evolution associated with the failure of granite under TDS conditions. As the confining pressure increases from 2 to 22 MPa, total energy accumulation shows a nonlinear growth trend, with the accumulation rate initially increasing and then decreasing. The evolution of elastic energy correlates with the stress–strain curve, while the proportion of dissipated energy to total energy gradually declines. This may be related to the peak postenergy release rate, where a higher release rate allows the sample to dissipate energy as kinetic energy, thereby reducing frictional energy loss. As the temperature increases from 30 to 110°C, compared to energy accumulation at ambient temperature, high temperature induces a shift from nonlinear to linear growth in total energy accumulation. The postpeak curves of elastic strain energy and dissipated energy become smoother, possibly indicating that high temperature influences the postpeak behavior of rock direct shear failure, resulting in reduced brittleness.

These observations highlight how confining pressure and temperature affect granite, leading to changes in postpeak failure behavior and brittleness characteristics. A plausible mechanism for temperature-induced postpeak mechanical behavior in granite is proposed, involving the synergistic effects of thermal expansion-induced microcracking and cement softening, which collectively promote brittle–ductile transition. This hierarchical coupling effect represents a core manifestation of the complexity in high-temperature rock mechanics. The differential thermal expansion coefficients of minerals (e.g., feldspar, mica) likely induce intergranular microcracks, reducing the overall rock stiffness and shifting energy accumulation from nonlinear (elastic-dominated) to linear (progressive damage-dominated) behavior. Simultaneously, thermal mismatch at grain boundaries generates new microcracks, advancing the initial damage accumulation stage and decreasing the proportion of nonlinear elastic energy storage. At elevated temperatures, cracks tend to propagate stably (subcritical growth) rather than through abrupt unstable propagation as observed at lower temperatures, resulting in reduced postpeak energy release rates and smoother dissipation curves. While these factors are challenging to quantify directly, Sections 3.2 and 3.3 attempt to elucidate this mechanism through fracture surface characteristics and energy evolution patterns.

The postpeak brittle fracture of hard brittle rocks is sudden and difficult to control; due to this uncertainty, the postpeak damage of rocks remains in a nonstationary state. The reason for this is the nonhomogeneity of rock materials and damage localization of the rock; the initial defects in the rock in the local stress concentration produce local deformation incoherence, which in turn causes the initial localization of damage of the rock. From the energy point of view, the postpeak fracture of a rock is a violent transformation from the high unstable energy at the peak to the low stable energy at the residual, and the fracture energy required for postpeak damage of a rock is a good depiction of this violent transformation of energy. The size of the fracture energy required for postpeak damage determines the brittleness characteristics of postpeak damage; therefore, the brittleness and the degree of brittleness can be analyzed and evaluated through the change of the fracture energy of postpeak damage.

The prepeak elastic strain energy can represent the energy storage capacity of the rock and the postpeak energy release rate can characterize the intensity of the rock rupture. Figure 8 shows the variation rules of the prepeak elastic strain energy and the postpeak energy release rate under different confining pressures and temperatures, and the results show that the confining pressure is increased from 2 to 22 MPa, and U_P^e and U^f show a linear increase law. A noteworthy phenomenon is that the intersection of U_P^e and U^f occurs when the confining pressure goes from low to high, and the significance of this intersection can represent whether the postpeak damage of the rock can occur spontaneously or not. When U_P^e is smaller than U^f, the postpeak damage of the rock needs the energy input from the outside in order to occur, and when U_P^e is larger than U^f, the postpeak damage of the rock can be carried out spontaneously. When the temperature increases from 30 to 110°C, U_P^e and U^f show a quadratic relationship, initially increasing and then decreasing.

The postpeak energy release rate and the prepeak elastic strain energy ratio can be used to represent the brittle characteristics of postpeak rupture of rocks. The energy ratio changes under different confining pressures and temperatures are shown in Figure 9. As the confining pressure is increased from 2 to 22 MPa, the energy ratio shows a decreasing trend, which indicates that the strong confinement state under high stress decreases the postpeak rupture brittleness of the rock (Figure 9a). As the temperature is increased from 30 to 110°C, the energy ratio shows a decreasing trend (Figure 9b), which indicates that the high-temperature effect also decreases the postpeak rupture brittleness of the rock. Damage brittleness decreases. Since the release and dissipation of postpeak energy are related to the damaged surface, and the damaged surface of rocks usually has a certain degree of randomness, which may include the influence of mineral composition, mineral grain size, and internal defects, and so on, to reduce the influence of this randomness to more accurately evaluate the postpeak brittleness of the rock damage, this study introduces the influence of the parameters of the damaged surface in the next part of the discussion.

3.3 | Characterization of damaged surface morphology

In this study, a quantitative evaluation of the damaged surface of the rock is carried out using the 3D scanner and the supporting software produced by Artec Space Spider Company (Figure 10); the 3D accuracy of the scanner 3D point precision is 0.05 mm, 3D resolution is 0.1 mm, and 3D accuracy over distance is 0.05 + 0.3 mm/m. The scanning results of the cross-section information with different confining pressures and temperatures are shown in Figure 11. The cloud diagrams represent the height information of the direct shear broken surface of different

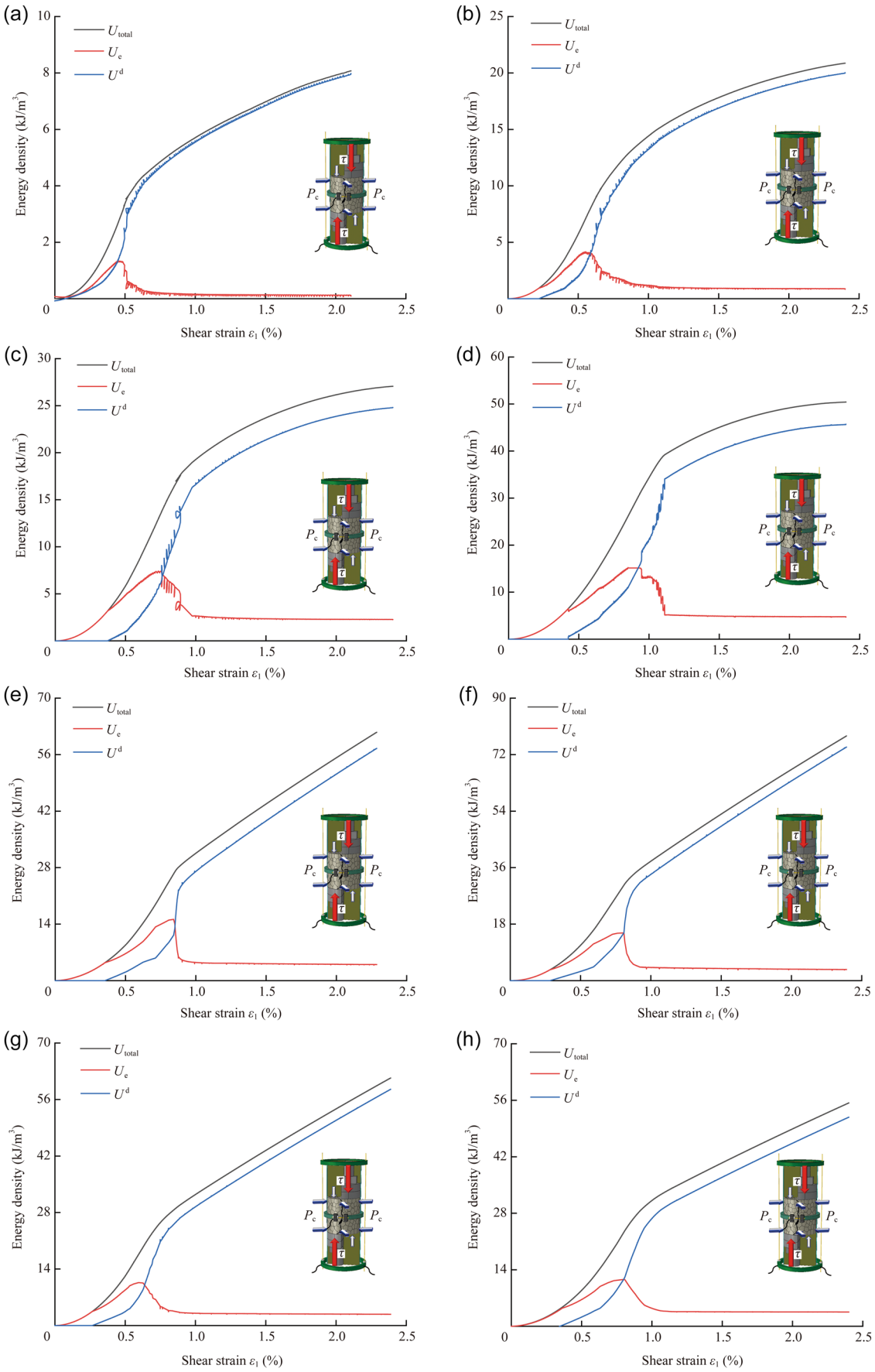

FIGURE 7 Energy evolution during the triaxial direct shear process of granite. (a) $T = 30°C$, $P_c = 2$ MPa, (b) $T = 30°C$, $P_c = 9$ MPa, (c) $T = 30°C$, $P_c = 15$ MPa, (d) $T = 30°C$, $P_c = 22$ MPa, (e) $T = 50°C$, $P_c = 22$ MPa, (f) $T = 70°C$, $P_c = 22$ MPa, (g) $T = 90°C$, $P_c = 22$ MPa, and (h) $T = 110°C$, $P_c = 22$ MPa.

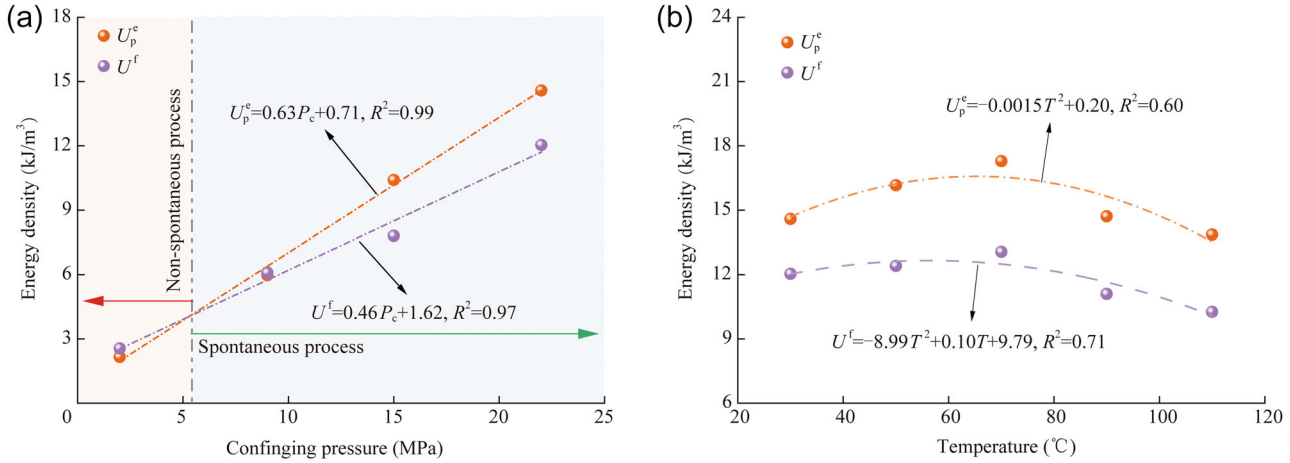

FIGURE 8 Variation of U_P^e and U^f: (a) U_P^e/U^f versus confining pressure and (b) U_P^e/U^f versus temperature.

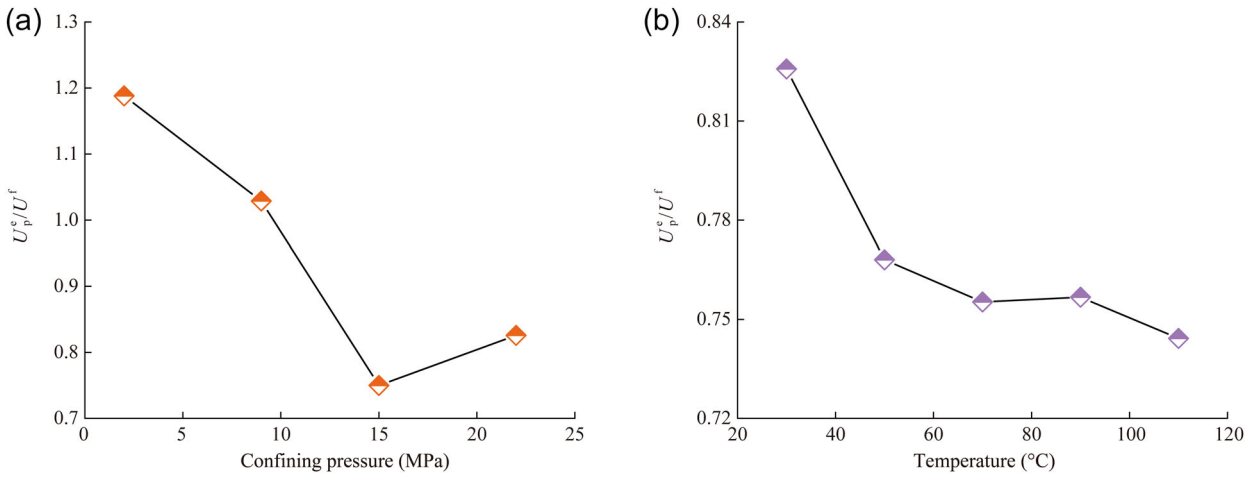

FIGURE 9 Variation of the energy ratio U_P^e/U^f: (a) U_P^e/U^f versus confining pressure and (b) U_P^e/U^f versus temperature.

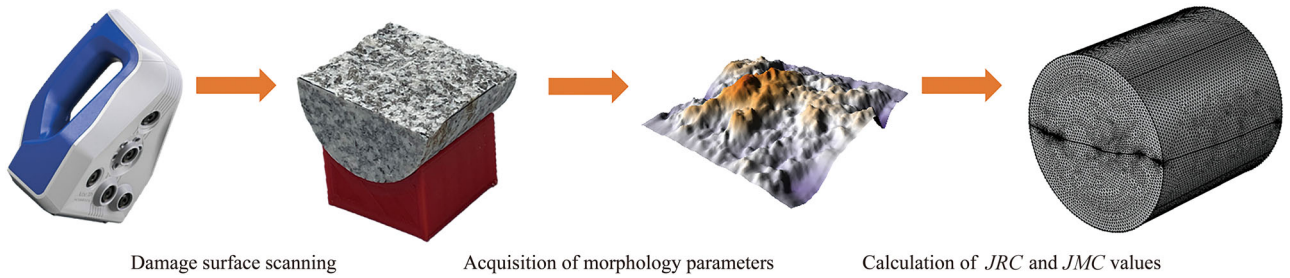

FIGURE 10 Access to damage surface information.

specimens, with a length and width of 50 mm × 50 mm, the shear direction from left to right, and the different color distributions represent the projections of the different heights in the plane.

JRC and *JMC* provide intuitive metrics for quantifying the shear characteristics of failure surfaces through the mapping relationship between the geometric morphology and mechanical response: *JRC* represents the contribution of "morphological complexity" to shear resistance, while *JMC* characterizes the influence of "contact effectiveness" on energy distribution. Together, they systematically explain the temperature-induced evolution of failure surface behavior, such as energy mode transitions and postpeak smoothing, serving as a critical bridge connecting microstructural changes to macroscopic mechanical responses. Figure 12 shows the change rule of *JRC* and *JMC* of the damaged surface of the specimen under different confining pressures, and the results show that the *JRC* of the damaged surface decreases slightly with the increase of the confining pressure, and the value of *JMC* of the damaged surface increases with the increase of the confining pressure. The reason for this phenomenon may be that the constraining effect of the confining pressure causes an increase in the

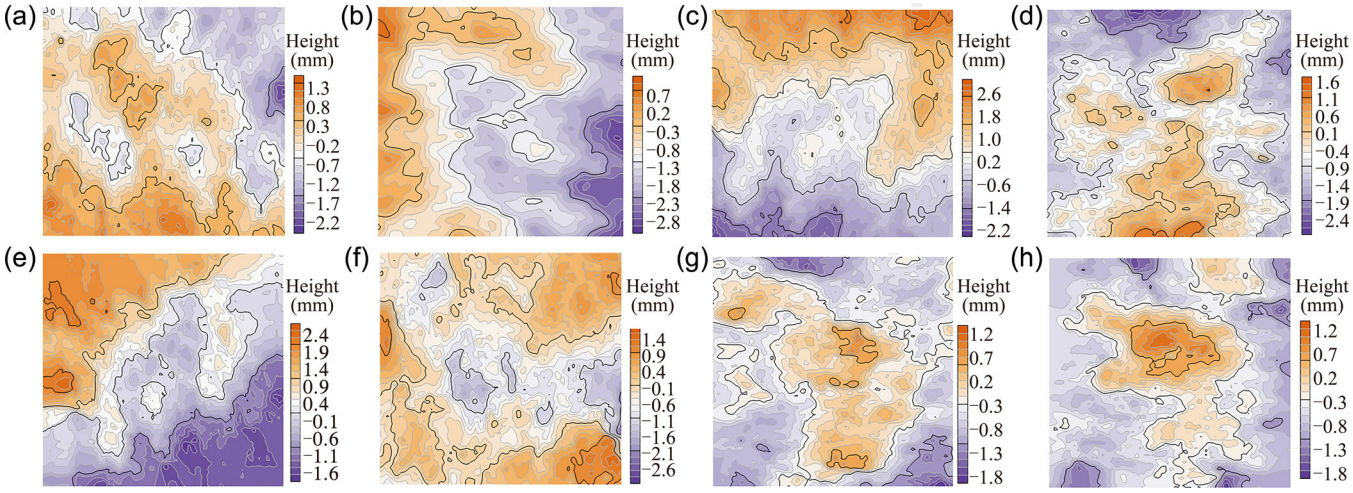

FIGURE 11 Results of section information scanning: (a) $T = 30°C$, $P_c = 2$ MPa, (b) $T = 30°C$, $P_c = 9$ MPa (c) $T = 30°C$, $P_c = 15$ MPa, (d) $T = 30°C$, $P_c = 22$ MPa, (e) $T = 50°C$, $P_c = 22$ MPa, (f) $T = 70°C$, $P_c = 22$ MPa, (g) $T = 90°C$, $P_c = 22$ MPa, and (h) $T = 110°C$, $P_c = 22$ MPa (The legend represents the height in the z-direction in mm, with 25 mm from the bottom of the specimen as the reference plane).

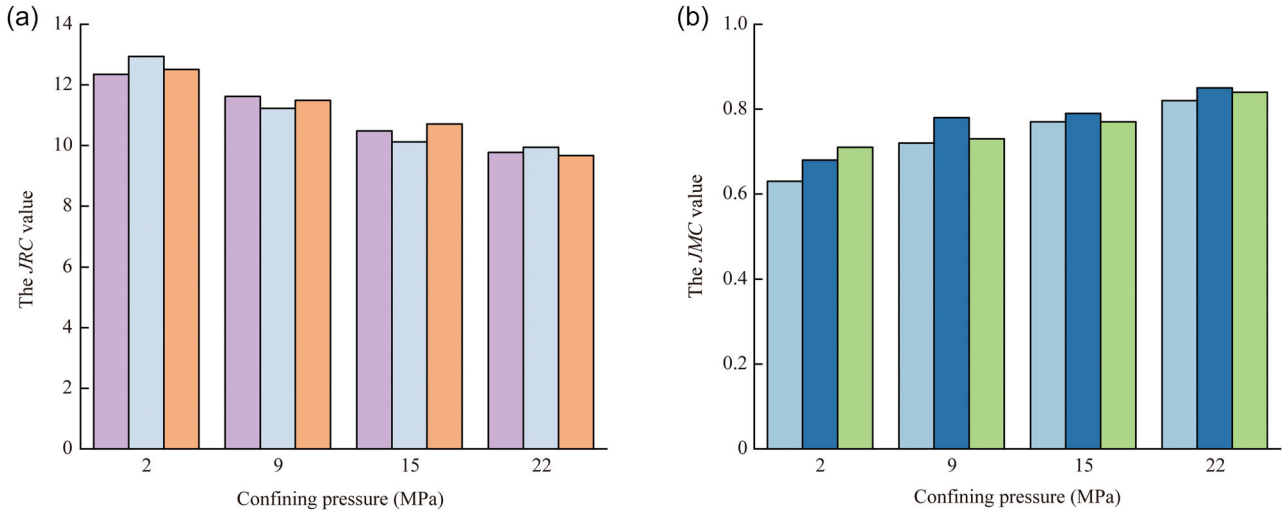

FIGURE 12 *JRC* values and *JMC* values versus confining pressure: (a) *JRC* versus pressure and (b) *JMC* versus pressure.

perforation damage, which reduces the *JRC* value of the damaged surface, and the high confining pressure increases the contact friction behavior between the damaged surfaces, so the *JMC* value of the damaged surfaces increases with it.

The change rule of *JRC* and *JMC* of the damaged surface of the specimen at different temperatures is shown in Figure 13, and the results show that the *JRC* of the damaged surface decreases slightly with the increase of the temperature, and the change of the *JMC* value of the damaged surface with the temperature is not obvious. With the same trend of the influence of the confining pressure on the damaged surface, the increase in temperature also caused a downward trend in the *JRC* value of the damaged surface, which may be attributed to the incongruity of the thermal expansion effect between minerals to promote the proportion of perforation damage and the thermal cracking behavior between minerals caused by the decrease in the *JRC* value of the damaged surface, while the *JMC* is mainly affected by the shear rate and friction behavior of the damaged surface and the damage surface friction behavior of the damaged surface is mainly affected by the shear rate and friction behavior of the damaged surface. The friction behavior between the surfaces did not change much, so the *JMC* values of the damaged surfaces did not show significant changes.

Rough surfaces (high *JRC*) are prone to brittle failure, such as dilation and fracture, while smooth surfaces (low *JRC*) tend to show steady-state sliding, directly influencing the nonlinear characteristics of energy release. High temperatures may alter surface roughness through thermal expansion or mineral decomposition, such as microcrack blunting or mineral softening, thereby explaining the transition in energy accumulation patterns through *JRC* changes. The geometric conformity between the upper and lower

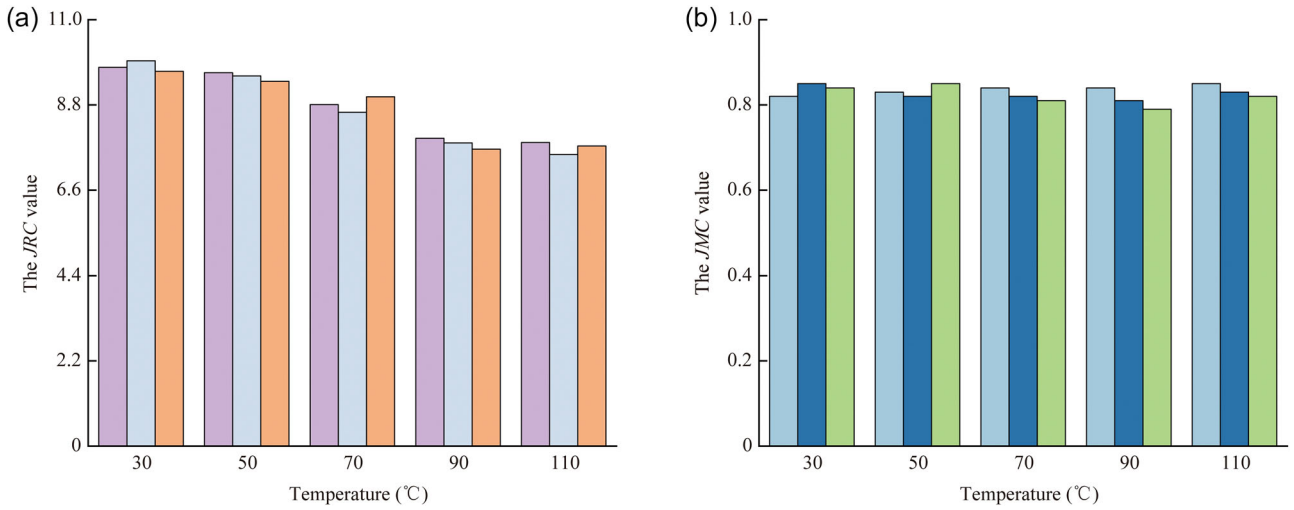

FIGURE 13 *JRC* values and *JMC* values versus temperature: (a) *JRC* versus temperature and (b) *JMC* versus temperature.

surfaces of the failure plane, characterized by the proportion and spatial alignment of contact areas, is critical. High *JMC* values, indicating good matching, result in larger actual contact areas and more uniform frictional resistance, leading to smoother energy dissipation. Conversely, low *JMC* values cause localized stress concentration and sudden slip. Poorly matched joints (low *JMC*) are susceptible to stress drops due to interlocking failure in the postpeak stage, while well-matched joints (high *JMC*) show gradual sliding, directly correlating with the observed smoothing of postpeak curves in experiments. At elevated temperatures, rock may experience thermal expansion differences, leading to reduced matching (lower *JMC*) or mineral melting filling gaps (higher *JMC*). However, since the temperature in this study remains relatively low compared to the melting points of the minerals, *JMC* does not show significant changes.

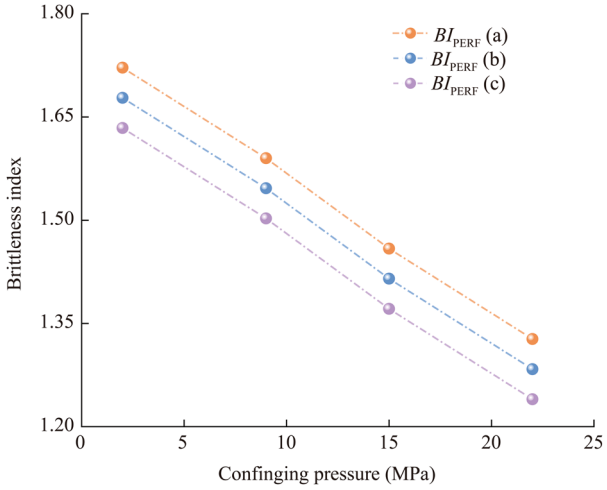

FIGURE 14 Variation of the brittleness index (BI_{PERF}) with the confining pressure.

4 | DISCUSSION

4.1 | Verification of the reliability of BI_{PERF}

To verify the reliability of the new brittleness index proposed in this study, the applicability to direct shear damage, and the evaluation effect of rock brittleness at high temperatures, eight widely used brittleness index evaluation methods are selected for comparative verification, and the calculation results are shown in Table 3. The new brittleness index BI_{PERF} can be obtained using the formula in part.2 and the experimental data in part.3, and the reliability of the new index is verified. Previous research has confirmed that in the triaxial test, the increase of the confining pressure will reduce the brittleness of the rock and make it almost ductile. This study validates the newly proposed brittleness index by applying the principle that increasing confining pressure reduces rock brittleness. Figure 14 shows the BI_{PERF} values under confining pressures of 2, 9, 15, and 22 MPa, and the results show that when the confining pressure increases, the brittleness value reflected by the BI_{PERF} value decreases; The results demonstrate that the newly proposed brittleness index effectively captures the trend of reduced rock brittleness under increasing confining pressure, so it can be concluded that the BI_{PERF} value can accurately evaluate the brittleness of the rock.

4.2 | Comparison with other brittleness indexes

The average of the three repetitions of the test was obtained and is shown in Figure 15, and the changes in the brittleness index under various brittleness calculation methods affected by different confining pressures are also shown. The results show that the existing brittleness evaluation indexes do not describe the brittleness changes of rocks under TDS conditions well. BI_{13}, BI_{14}, BI_{15}, and BI_{18} show no obvious change with the increase of the confining pressure because only the peak characteristics of stress–strain are considered in the calculation methods, and the postpeak behavior is not taken into account. Surprisingly, the variations in BI_{19} and BI_{20} contradict

TABLE 3 Calculated results of the brittleness index.

Number	B_{11}	B_{12}	B_{13}	B_{14}	B_{15}	B_{18}	B_{19}	B_{20}	B_{PERF}
BSSRT-01a	0.72	0.56	0.09	0.13	0.87	0.37	0.70	0.47	1.72
BSSRT-01b	0.70	0.53	0.09	0.13	0.87	0.38	0.80	0.52	1.68
BSSRT-01c	0.73	0.54	0.09	0.13	0.87	0.39	0.77	0.49	1.63
BSSRT-02a	0.65	0.49	0.09	0.13	0.87	0.38	0.70	0.46	1.59
BSSRT-02b	0.58	0.46	0.09	0.13	0.87	0.42	0.85	0.51	1.55
BSSRT-02c	0.65	0.48	0.09	0.13	0.87	0.47	0.99	0.53	1.50
BSSRT-03a	0.63	0.44	0.08	0.13	0.87	0.41	0.90	0.55	1.46
BSSRT-03b	0.68	0.42	0.08	0.13	0.87	0.46	1.36	0.66	1.41
BSSRT-03c	0.63	0.43	0.08	0.13	0.87	0.44	1.17	0.62	1.37
BSSRT-04a	0.57	0.35	0.08	0.13	0.87	0.43	1.00	0.57	1.33
BSSRT-04b	0.61	0.45	0.08	0.13	0.87	0.42	0.99	0.57	1.28
BSSRT-04c	0.65	0.48	0.08	0.13	0.87	0.42	0.99	0.57	1.24
BSSHM-01a	0.43	0.18	0.08	0.14	0.86	0.41	0.89	0.54	2.40
BSSHM-01b	0.59	0.24	0.11	0.16	0.84	0.45	1.07	0.58	2.04
BSSHM-01c	0.59	0.21	0.11	0.15	0.85	0.45	1.07	0.58	2.06
BSSHM-02a	0.52	0.21	0.06	0.10	0.90	0.42	0.96	0.56	2.16
BSSHM-02b	0.58	0.26	0.12	0.18	0.82	0.43	1.01	0.57	1.98
BSSHM-02c	0.57	0.26	0.05	0.08	0.92	0.44	1.02	0.57	1.97
BSSHM-03a	0.55	0.26	0.08	0.14	0.86	0.41	0.88	0.53	2.18
BSSHM-03b	0.55	0.19	0.10	0.14	0.86	0.44	1.05	0.58	1.86
BSSHM-03c	0.56	0.15	0.11	0.16	0.84	0.45	1.13	0.60	1.69
BSSHM-04a	0.50	0.14	0.11	0.17	0.83	0.41	0.90	0.55	2.17
BSSHM-04b	0.63	0.20	0.10	0.12	0.88	0.45	1.11	0.59	1.83
BSSHM-04c	0.61	0.20	0.09	0.12	0.88	0.47	1.17	0.60	1.66

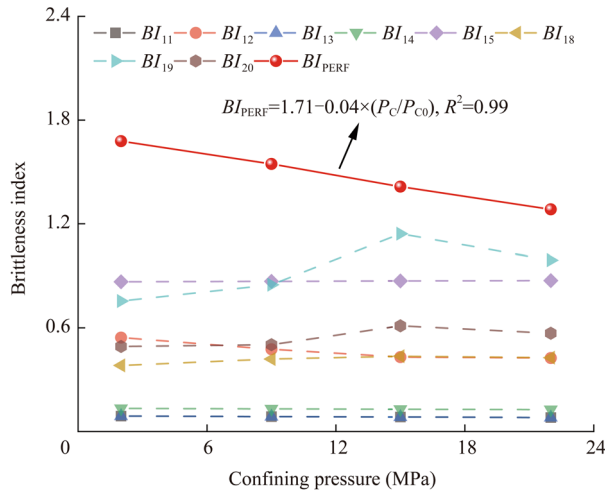

FIGURE 15 Effectiveness of different brittleness calculation methods for direct shear damage of granite.

the established principle that high confining pressure reduces rock brittleness, which indicates that the brittleness calculation methods for rock compression conditions do not apply to shear conditions. BI_{11} and BI_{12} are not sensitive to the change in the confining pressure, although they show a tendency to decrease with the confining pressure. It seems that BI_{11} and BI_{12} do not take into account the effect of the damaged surface, although they take into account the postpeak parameters. Through the analysis of the *JRC* and *JMC* values in Section 3.3, it is found that there is an obvious correlation between *JRC* and *JMC* values in terms of the confining pressure and temperature. After the introduction of the *JRC* and *JMC* values, BI_{PERF} shows a decreasing trend with the increase of the confining pressure. It can characterize well the brittleness of the rock with the change of the confining pressure. As the confining pressure increases from 2 to 22 MPa, BI_{PERF} decreases by 23.50%.

4.3 | Brittleness at high temperatures in real time

The variation of the brittleness index under various brittleness calculation methods at different temperatures is shown in Figure 16. The experimental results show that calculation methods other than BI_{PERF} cannot capture the brittleness characteristics of rocks at high temperatures. The possible reason is that the main discriminating

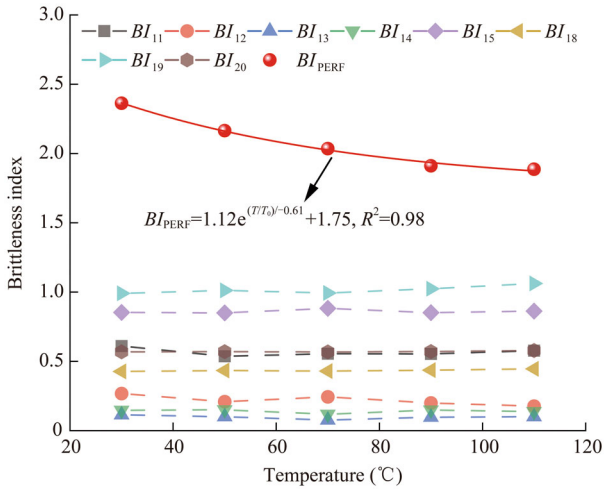

FIGURE 16 BI_{PERF} of direct shear damage of Beishan granite at different temperatures.

parameters of these calculation methods are the characteristic stress and the characteristic strain; however, the characteristic stress and the characteristic strain are not sensitive to the effect of moderately high temperatures, and BI_{PERF} can better characterize the brittleness of the rock as a function of temperature, which takes into account the *JRC* and *JMC* values that characterize the damage surfaces. As the temperature increases from 30 to 110°C, BI_{PERF} decreases by 20.16%.

5 | CONCLUSION

In this study, a new type of rock brittleness evaluation index considering the characteristics of the damaged surface and the postpeak energy release rate was proposed, and its reliability and accuracy were verified by TDS experiments under high temperature and high pressure with Beishan granite. Also, the influence of the confining pressure and temperature on the postpeak energy release rate of the granite damaged by direct shear was determined. Three-dimensional laser scanning technology was used to obtain the characteristic parameters of the confining pressure and temperature on the damage surface. Based on the experimental results, the following main conclusions were drawn in the range of confining pressure from 2 to 22 MPa and temperature from 30 to 110°C:

1. The postpeak energy release rate shows a linear positive correlation with confining pressure. As the confining pressure increases from 2 to 22 MPa, the postpeak energy release rate increases by 3.72 times. With increasing temperature, the postpeak energy release rate initially increases and then decreases, reaching its maximum at 70°C, which is 108.7% of the value at 30°C.
2. The *JRC* values are negatively correlated with the confining pressure and temperature, and the temperature and confining pressure affected the *JRC* values to a similar extent. The temperature, however, has no significant effect on the *JMC* values.
3. A new brittleness index is established by taking into account the damaged surface characteristics and the postpeak energy release rate. The new brittleness index is scientifically defined and simple to calculate. The reliability of the proposed new brittleness index is verified by a series of TDS tests, and by comparing the results with those of the other eight brittleness indexes, the results prove that the new evaluation index is more accurate for brittleness evaluation of direct shear damage of rocks under different confining pressures, and it can be popularized and applied in the engineering field.
4. Comparison of other brittleness indices with BI_{PERF} for characterizing the direct shear failure of Beishan granite under varying confining pressures and temperatures demonstrates that BI_{PERF} shows clearer trends and more accurate results. The findings confirm that the brittleness of Beishan granite decreases with increasing confining pressure, with BI_{PERF} declining by 23.5% as the confining pressure increases from 2 to 22 MPa. Similarly, brittleness decreases with increasing temperature, with BI_{PERF} decreasing by 20.16% as the temperature increased from 30 to 110°C.

It should be noted that the brittleness index proposed in this article has only been validated for Beishan granite under conditions of 30 to 110°C in the context of nuclear waste disposal. Future work will focus on assessing its applicability to a broader range of rock types and high temperatures.

AUTHOR CONTRIBUTIONS

Biao Wang: Methodology; experiment; validation; writing—original draft preparation. **Zaobao Liu**: Conceptualization; methodology; investigation; writing—draft preparation and edition; supervision. **Jing Xue**: Discussion and review. **Bo Lu**: Discussion; reviewing and editing. **Wei Zeng**: Validation; investigation. **Dengke Zhang**: Validation; investigation.

ACKNOWLEDGMENTS

This study was supported by the Natural Science Foundation of China (52278333) and the China Atomic Energy Authority (CAEA) for China's URL Development Program, the Geological Disposal Program.

CONFLICT OF INTEREST STATEMENT

The authors declare no conflicts of interest.

DATA AVAILABILITY STATEMENT

The data that support the findings of this study are available on request from the corresponding author. The data are not publicly available due to privacy or ethical restrictions.

ORCID

Biao Wang https://orcid.org/0000-0002-7394-6097

REFERENCES

Altindag R. The evaluation of rock brittleness concept on rotary blast hold drills. *J South Afr Inst Min Metallur*. 2002;102:61-66.

Altindag R. Correlation of specific energy with rock brittleness concepts on rock cutting. *J South Afr Inst Min Metallur*. 2003;103:163-171.

Altindag R. Assessment of some brittleness indexes in rock-drilling efficiency. *Rock Mech Rock Eng*. 2010;43:361-370.
Andreev GE. *Brittle Failure of Rock Materials: Test Results and Constitutive Models*. CRC Press; 1995.
Barton N. The shear strength of rock and rock joints. *Int J Rock Mech Min Sci*. 1976;13(9):255-279.
Bishop AW. Progressive failure with special reference to the mechanism causing it. *Proc Geotech Conf*. 1967;2:142-150.
Chen L, Zhao X, Liu J, et al. Progress on rock mechanics research of Beishan granite for geological disposal of high-level radioactive waste in China. *Rock Mech Bull*. 2023;2:100046.
Feng G, Ma Q, He Z, et al. Time-delayed failure process of granite and its energy evolution and acoustic emission characteristics. *Eng Failure Anal*. 2024;157:107854.
Gong F, Wang Y. A new rock brittleness index based on the peak elastic strain energy consumption ratio. *Rock Mech Rock Eng*. 2022;55:1571-1582.
Gong F, Zuo Y, Luo S, Wang Y. An improved method to calculate the rock brittleness index PEECR based on linear energy storage law. *Deep Resour Eng*. 2024;1:100005.
Gong X, Sun CC. A new tablet brittleness index. *Eur J Pharmaceut Biopharmaceut*. 2015;93:260-266.
Hajiabdolmajid V, Kaiser P. Brittleness of rock and stability assessment in hard rock tunneling. *Tunnel Undergr Space Technol*. 2003;18:35-48.
He M, Huang B, Zhu C, Chen Y, Li N. Energy dissipation-based method for fatigue life prediction of rock salt. *Rock Mech Rock Eng*. 2018;51:1447-1455.
Heinze T, Frank S, Wohnlich S. FSAT—A fracture surface analysis toolbox in MATLAB to compare 2D and 3D surface measures. *Comput Geotech*. 2021;132:103997.
Hucka V, Das B. Brittleness determination of rocks by different methods. *Int J Rock Mech Min Sci Geomech Abstr*. 1974;11:389-392.
Jarvie DM, Hill RJ, Ruble TE, Pollastro RM. Unconventional shale-gas systems: the Mississippian Barnett Shale of north-central Texas as one model for thermogenic shale-gas assessment. *Am Assoc Pet Geol Bull*. 2007;91:475-499.
Jin X, Shah SN, Roegiers JC, Zhang B. An integrated petrophysics and geomechanics approach for fracability evaluation in shale reservoirs. *SPE J*. 2015;20:518-526.
Kahraman S, Altindag R. A brittleness index to estimate fracture toughness. *Int J Rock Mech Min Sci*. 2004;41:343-348.
Kidybiński A. Bursting liability indices of coal. *Int J Rock Mech Min Sci Geomech Abstr*. 1981;18:295-304.
Lawn BR, Marshall DB. Hardness, toughness, and brittleness: an indentation analysis. *J Am Ceram Soc*. 1979;62:347-350.
Liang L, Liu X, Xiong J, Wu T, Ding Y. New model to evaluate the brittleness in shale formation. *Int Geophys Conf*. 2017;1248-1251.
Liu B, Liu Z, Zhang M, Xu J, Hao L. Triaxial direct shear properties, cohesive damage behavior and shear constitutive model of sandstone under high confining pressure. *Eur J Environ Civil Eng*. 2023;28:1284-1299.
Liu Z, Wang C, Zhang M, Shao J. Cracking property and brittleness evaluation of granite under high-temperature true triaxial compression in geothermal systems. *Geomech Geophys Geo Energy Geo Res*. 2023;9:99.
Meng F, Wong LNY, Zhou H. Rock brittleness indices and their applications to different fields of rock engineering: a review. *J Rock Mech Geotech Eng*. 2021;13:221-247.
Meng F, Zhou H, Zhang C, Xu R, Lu J. Evaluation methodology of brittleness of rock based on post-peak stress–strain curves. *Rock Mech Rock Eng*. 2015;48:1787-1805.
Munoz H, Taheri A, Chanda EK. Fracture energy-based brittleness index development and brittleness quantification by pre-peak strength parameters in rock uniaxial compression. *Rock Mech Rock Eng*. 2016;49:4587-4606.
Nejati HR, Moosavi SA. A new brittleness index for estimation of rock fracture toughness. *J Min Environ Earth Sci*. 2017;8:83-91.
Quinn JB, Quinn GD. Indentation brittleness of ceramics: a fresh approach. *J Mater Sci*. 1997;32:4331-4346.
Rahimzadeh Kivi I, Ameri M, Molladavoodi H. Shale brittleness evaluation based on energy balance analysis of stress-strain curves. *J Petrol Sci Eng*. 2018;167:1-19.
Sehgal J, Nakao Y, Takahashi H, Ito S. Brittleness of glasses by indentation. *J Mater Sci Lett*. 1995;14:167-169.
Seo E, Kim KI, Yoo H, Yoon J, Min KB. Far-field analysis of shear slip potential and ground uplift by high-level radioactive waste repositories with single- and multi-canister and multi-layer disposal concepts. *Tunnel Undergr Space Technol*. 2024;145:105611.
Singh SP. Brittleness and the mechanical winning of coal. *Min Sci Technol*. 1986;3:173-180.
Tarasov BG. Fan-hinged shear instead of frictional stick–slip as the main and most dangerous mechanism of natural, induced, and volcanic earthquakes in the earth's crust. *Deep Undergr Sci Eng*. 2023;2:305-336.
Wang F, Gale J. Screening criteria for shale-gas systems. *Gulf Coast Assoc Geol Soc Trans*. 2009;59:779-793.
Wang S, Tang Y, Wang S. Influence of brittleness and confining stress on rock cuttability based on rock indentation tests. *J Central South Univ*. 2021;28:2786-2800.
Wang S, Zhao W, Fu X, Zhang Z, Wang T, Ge J. A universal method for quantitatively evaluating rock brittle-ductile transition behaviors. *J Petrol Sci Eng*. 2020;195:107774.
Wang Y, Tang P, Li P, Xia Y. Effect of disturbed frequency on rock failure and energy characteristics exposed to triaxial fatigue and multistage unloading confining pressure (TF-MSUCP) conditions. *Eng Failure Anal*. 2023;145:106997.
Xie H, Li L, Ju Y, Peng R, Yang Y. Energy analysis for damage and catastrophic failure of rocks. *Sci China Technol Sci*. 2011;54:199-209.
Yarali O, Kahraman S. The drillability assessment of rocks using the different brittleness values. *Tunnel Undergr Space Technol*. 2011;26:406-414.
Zhang D, Huang A, Ma H, et al. Exploring damage evolution of rock under different penetration and cutter spacing conditions using finite-discrete element method. *Comp Geotech*. 2024;173:106573.
Zhang D, Ranjith PG, Perera MSA. The brittleness indices used in rock mechanics and their application in shale hydraulic fracturing: a review. *J Petrol Sci Eng*. 2016;143:158-170.
Zhang H, Xu B, Liu J, Guo B, Sun H, Yang Q. SDHB reduction promotes oral lichen planus by impairing mitochondrial respiratory function. *Ann Transl Med*. 2022;10:1367.
Zhang Y, Feng XT, Yang C, Zhang X, Sharifzadeh M, Wang Z. Fracturing evolution analysis of Beishan granite under true triaxial compression based on acoustic emission and strain energy. *Int J Rock Mech Min Sci*. 2019;117:150-161.
Zhao J. Joint surface matching and shear strength part B: JRC-JMC shear strength criterion. *Int J Rock Mech Min Sci*. 1997;34:179-185.
Zhao K, Yu X, Zhou Y, Wang Q, Wang J, Hao J. Energy evolution of brittle granite under different loading rates. *Int J Rock Mech Min Sci*. 2020;132:104392.
Zhao XG, Wang J, Cai M, Su GS. Influence of intermediate principal stress on the strainburst characteristics of Beishan granite with consideration of end effect. *Rock Mech Rock Eng*. 2021;54:4771-4791.

How to cite this article: Wang B, Liu Z, Xue J, Lu B, Zeng W, Zhang D. A rock brittleness index based on the postpeak energy release rate and damage surface characteristics for brittle hard rock. *Deep Undergr Sci Eng*. 2025;1-15. doi:10.1002/dug2.70058

APPENDIX A

Triaxial direct shear stress–strain curve of Beishan granite.

See Figure A1.

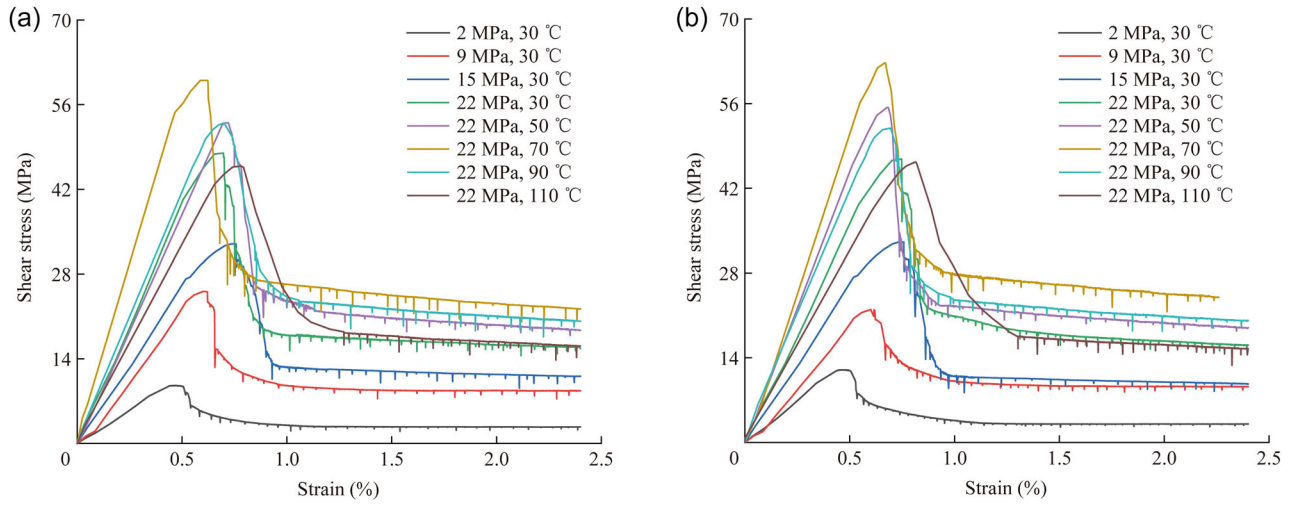

FIGURE A1 Triaxial direct shear stress–strain curves of Beishan granite. (a) Repeat test 1 and (b) Repeat test 2.

AUTHOR BIOGRAPHY

Prof. Zaobao Liu currently serves as the vice dean of the School of Resources and Civil Engineering at Northeastern University in Shenyang, China. Additionally, he serves as the executive deputy director of the Key Laboratory of the Ministry of Education on Safe Mining of Deep Metal Mines in China. His research interests cover high-temperature rock mechanics, seepage mechanics of unconventional geological reservoirs, geological disposal of high-level radioactive waste, and deep energy mining. He has been awarded the Changjiang Scholars Program and the first-class prize of the Science & Technology Progress Award of the Chinese Society of Rock Mechanics and Engineering (CSRME). He has served as the coordinating investigator on numerous research projects funded by the Natural Science Foundation of China, the China Ministry of Science and Technology, Liaoning Province, China. He currently holds the position of chairman of the Cold Region Geomechanics and Engineering Commission and vice chairman of the Multifield Coupling Commission of CSRME, and is an editorial board member of the *Journal of Rock Mechanics and Geotechnical Engineering*, and *Geotechnical and Geological Engineering*.